POLITECNICO DI TORINO
Repository ISTITUZIONALE

High-accuracy graphene quantum Hall array resistance standards based on wye-delta transformation

Original
High-accuracy graphene quantum Hall array resistance standards based on wye-delta transformation / Lin, W., Oe, T., Musso, M., Jarrett, D.G., Panna, A.R., Steffens, K.L., Tran, N.T.M., Ortolano, M., Yang, C., Liang, C., Rigosi, A.F., Elmquist, R.E., Yang, Y.. - In: NPJ 2D MATERIALS AND APPLICATIONS. - ISSN 2397-7132. - (2026). [10.1038/s41699-026-00749-3]

Availability:
This version is available at: 11583/3017839 since: 2026-11-12T13:20:05Z

Publisher:
Nature

Published
DOI:10.1038/s41699-026-00749-3

Terms of use:

This article is made available under terms and conditions as specified in the corresponding bibliographic description in the repository

Publisher copyright

(Article begins on next page)

21 November 2026

npj | 2D materials and applications

Article

Published in partnership with FCT NOVA with the support of E-MRS

Article in Press

https://doi.org/10.1038/s41699-026-00749-3

High-accuracy graphene quantum Hall array resistance standards based on wye-delta transformation

Check for updates

Wei-Chen Lin[1,2], Takehiko Oe[1,3], Marta Musso[1,4], Dean G. Jarrett[1], Alireza R. Panna[1], Kristen L. Steffens[1], Ngoc Thanh Mai Tran[1,5], Massimo Ortolano[4], Cheng-Hsueh Yang[6], Chi-Te Liang[6], Albert F. Rigosi[1], Randolph E. Elmquist[1] & Yanfei Yang[1] ✉

The wye-delta (Y-Δ) transformation has been demonstrated to significantly reduce the number of Hall bars necessary for high-resistance quantum Hall array resistance standards (QHARS), addressing the spatial limitation in the practical applications. Network designs have been described for graphene-based Y-Δ arrays to realize resistance values of $77\,\frac{h}{2e^2}$ (≈ 1 MΩ), $775\,\frac{h}{2e^2}$ (≈ 10 MΩ), and $7748\,\frac{h}{2e^2}$ (≈ 100 MΩ). A programmable QHARS is conceived based on a Y-network with multiple arms. We will present the magnetoresistance transport properties of Y-Δ array devices, followed by the precision measurements of three identical devices, each consisting of 28 Hall bars. At 1.6 K, two devices are quantized at $77\,\frac{h}{2e^2}$ (≈ 1 MΩ) to within 80 nΩ/Ω at magnetic field as low as 5 T and 6 T, respectively. Such high accuracy is achieved without cryogenic current comparator, but through a solution with core components comprising the triple-connections to the three terminals of the Y-Δ array device, a dual source bridge (DSB), and a substitution method. Our results establish the viability to develop a LHe-free QHR system with accuracy of a few parts in 10^8 for high-resistance calibration. This system would be readily adoptable to improve traceability and reduce the calibration chain for industrial applications.

Reliable and accurate electrical resistance standards are crucial for a wide range of applications from scientific research and manufacturing to safety and quality control. To ensure consistency and reliability in electrical measurements, all electrical resistance standards are ultimately traceable to national and international quantum Hall resistance standards (QHRS) that are linked to two fundamental physical constants, namely the elementary charge e and the Planck constant h.

The quantum Hall effect (QHE) is a universal macroscopic quantum phenomenon that has been reported in various systems, including the inversion layer of a silicon metal-oxide-semiconductor field-effect transistor[1], III–V semiconductors[2], graphene[3], topological insulators[4], and transition-metal dichalcogenides (TMDs)[5]. It occurs in high magnetic fields and at low temperatures, where quantized Hall resistance plateaux are observed at integer or fractional values of the constant h/e^2. Since 1990, the GaAs/AlGaAs heterostructure has been instrumental in realizing QHRS because accuracy of a few parts in 10^9 can be measured repeatedly in these devices at the quantized resistance values of $h/2e^2$ and $h/4e^2$. To achieve such accuracy, a 3He refrigerator or dilution refrigerator is necessary to accommodate GaAs-based QHRS at <1.3 K or <0.3 K, respectively, where the $h/2e^2$ plateau is often measured at 10 T and the $h/4e^2$ measured at 5 T. Consuming large amount of liquid helium, these complicated and expensive systems are inaccessible to many scientific researchers and manufacturers.

In recent years, groundbreaking research on epitaxial graphene has been paving the way for broader adoption of QHRS in industrial settings. Graphene QHRS can be operated under relaxed experimental conditions at a temperature of 1.3 K and in magnetic field down to 3.5 T, or at a temperature of 10 K and in a magnetic field of 8.5 T 6. Therefore, the QHR system based on graphene devices can be simplified as a compact system comprising a closed cycle cryocooler and a 5 T superconducting magnet[6–8]. Without the demand for advanced skills or expensive liquid helium, graphene QHRS will revolutionize industrial resistance metrology, offering improved traceability and stability to enhance safety and quality control.

Despite the accuracy, GaAs-based QHRS offers two well-quantized resistance plateaus ($h/2e^2$ and $h/4e^2$), whereas graphene-based QHRS offers

[1]National Institute of Standards and Technology, 100 Bureau Drive, Gaithersburg, MD, USA. [2]Department of Engineering and System Science, National Tsing Hua University, Hsinchu, Taiwan. [3]National Metrology Institute of Japan (NMIJ), Advanced Industrial Science and Technology (AIST), 1-1-1 Umezono, Tsukuba, Ibaraki, Japan. [4]Politecnico di Torino, Torino, Italy. [5]Joint Quantum Institute, University of Maryland, College Park, MD, USA. [6]Graduate Institute of Applied Physics, National Taiwan University, Taipei, Taiwan. ✉e-mail: yanfei.yang@nist.gov

only one ($h/2e^2$) that can be measured with uncertainty within a few parts in 10^9. On the other hand, electrical resistance standards cover a very wide range of values from μΩ to PΩ. The calibration chain providing traceability to QHRS is long and time-consuming for lower and higher resistance standards. At the high resistance end, resistance measurements in the MΩ range and higher, such as insulation resistance testing, is a crucial practice to ensure safety and reliability in major industries such as pharmaceuticals, aerospace and defense, environmental monitoring, electronics and semiconductor manufacturing, as well as power generation and transmission. The needs of high resistance measurement with higher accuracy (at or above 10^{-6}) and therefore an accessible quantum resistance standard in the MΩ range or higher are continuously driven by factors such as safety regulation, miniaturization, high-frequency applications and preventive maintenance.

Research areas to expand the quantized resistance values include quantum Hall arrays, graphene *p-n* junctions 9, fractional QHE, etc. Among these efforts, quantum Hall array is an intuitive and effective resolution with prosperous development since the 1990s[10–25]. Two breakthrough research studies developed techniques to eliminate interconnection and contact resistance, which are indispensable for achieving the accuracy of a few parts in 10^9 in quantum Hall array devices[10,21]. In 1993, Delahaye demonstrated the multiple connection technique that significantly reduced the effect of contact resistance, including the imperfection of contacts to the two-dimensional material and the series resistance of the connection wires[10]. Twenty-six years later, Kruskopf et al. demonstrated a superconducting interconnection technique that greatly simplifies the fabrication of QHARS because it effectively eliminates the crossing leads, required by the multiple connection technique especially for series arrays, and the associated leakage currents[21].

On the other hand, extensive research has been conducted to advance the technology for graphene quantum Hall array devices, from material synthesis and characterization to device fabrication and doping[8,26–30]. Currently, processes have been developed to produce homogeneous monolayer graphene grown epitaxially on silicon carbide substrate at millimeter scale[6,27,31], large enough to accommodate a few hundred Hall bars. Despite the continued effort to scale up the epitaxial graphene beyond the centimeter scale, the size of the chip carrier and the sample space in the cryocooler also impose practical dimension limitations for QHARS. Increasing the number of Hall bars in a limited space leads to size reduction of individual Hall bars, where the former will reduce the fabrication yield and the later will degrade the performance of individual Hall bars in the QHARS. Utilizing series arrays, Advanced Industrial Science and Technology (AIST) has developed 1 MΩ and 10 MΩ QHARS based on GaAs/AlGaAs heterostructures, consisting of 79 or 88 Hall bars[16,19,22] and 775 Hall bars[20], respectively. The 1 MΩ GaAs QHARS is quantized to within 20 nΩ/Ω at 0.5 K and magnetic field above 9 T[22], when compared to NIST's quantized Hall resistance standard with a cryogen current comparator. Recently, NIST has demonstrated that the wye-delta (Y-Δ) transformation is an efficient tool to reduce the required number of Hall bars in QHARS for resistances higher than 1 MΩ[25]. In this previous work, a prototype device consisting of a total 79 graphene Hall bars was utilized to produce 20.6 MΩ, a resistance value that would require 1596 Hall bars in a pure series network.

In this work, we will describe the optimization of Y-Δ arrays for graphene QHARS with quantized resistance values near 1 MΩ, 10 MΩ, and 100 MΩ and conceive a programmable QHARS utilizing a multiple-branch Y-network. Then we will present measurements of multiple Y-Δ array devices, including the magnetoelectric transport properties and the precision measurement by a dual source bridge. The graphene devices are held in a liquid helium cryostat with a base temperature of 1.6 K and a superconducting magnet of 9 T.

Results

Y-Δ transformation for quantum Hall array resistance standard

The wye-delta transformation[32] is a well-known mathematical technique to simplify complex circuits, widely used in the analysis of three-phase electric power circuits. In the electrical calibration community, the wye-delta transformation, usually the transformation from a "Y"-shaped network to a "Δ"-shaped network, is adopted to generate ultra-high resistance standards in the range from MΩ to PΩ[25,33–35].

As shown in Fig. 1(a), the Y-network (the orange schematic) and the Δ-network (the green schematic) connect three terminals A, B, and C. The Y-network has an extra node (O) in the center. The equivalence between the Y-network and the Δ-network is reflected in Eqs. (1)–(3), which are used to convert resistance values between each pair of the nodes from the Y-network to the Δ-network.

$$R_A = R_2 + R_3 + \frac{R_2 R_3}{R_1} \tag{1}$$

$$R_B = R_1 + R_3 + \frac{R_3 R_1}{R_2} \tag{2}$$

$$R_C = R_1 + R_2 + \frac{R_1 R_2}{R_3} \tag{3}$$

If the Y-network is built with physical resistors, then resistors (R_A, R_B, R_C) in the Δ-network are virtual resistors whose values can be measured by a dual source bridge. Figure 1(b) shows the Y-network for high resistance graphene Y-Δ array device, identified by the triplet (m_1, m_2, m_3). To scale up the equivalent resistance R_C, series arrays are chosen for R_1 (arm A) and R_2 (arm B) and a parallel array is chosen for R_3 (arm C) in the Y-network so that

$$R_1 = m_1 R_H \tag{4}$$

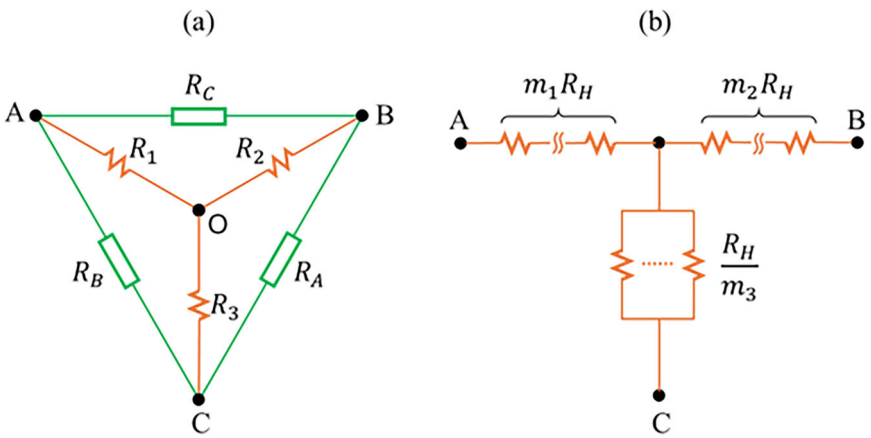


Fig. 1 | Diagram of Y-Δ transformation. **a** Schematic diagram for conventional Y-Δ transformation. **b** Schematic diagram for Y-Δ transformation with graphene Hall bar elements.

$$R_2 = m_2 R_H \tag{5}$$

$$R_3 = \frac{1}{m_3} R_H \tag{6}$$

where m_1, m_2, and m_3 are the number of Hall bars in the three arms of the Y-network, respectively. $R_H = \frac{h}{2e^2}$ is the quantized resistance of the $\nu = 2$ plateau in graphene that is robust for metrology application[36]. Substituting Equations (4)-(6) into Eq. (3), we have

$$R_C = (m_1 m_2 m_3 + m_1 + m_2) R_H = m_{WD} R_H \tag{7}$$

where $m_{WD} = m_1 m_2 m_3 + m_1 + m_2$ is an integer. We define the difference between R_C and the target resistance value (R_T) as $\delta_T = R_C - R_T$. Table 1 shows the Y-network configurations (m_1, m_2, m_3) with minimum δ_T for target resistances 1 MΩ, 10 MΩ, and 100 MΩ, under the condition of $(m_1 + m_2 + m_3) < 80$, where δ_T are –6207 μΩ/Ω, 246 μΩ/Ω, and –12 μΩ/Ω, for 1 MΩ, 10 MΩ, and 100 MΩ, respectively.

Table 1 | Y-networks for 1 MΩ, 10 MΩ,100 MΩ graphene Y-Δ array device

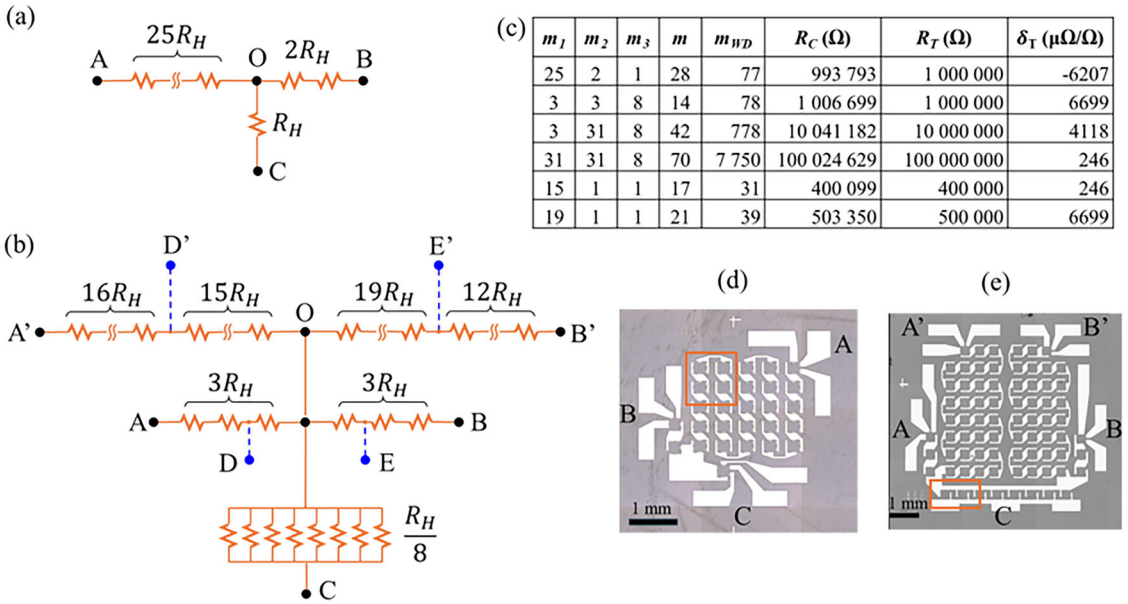
m_1	m_2	m_3	m	m_{WD}	R_C (Ω)	R_T (Ω)	δ_T (μΩ/Ω)
38	1	1	40	77	993,793	1,000,000	–6207
25	2	1	28	77	993,793	1,000,000	–6207
12	5	1	18	77	993,793	1,000,000	–6207
15	2	2	19	77	993,793	1,000,000	–6207
19	1	3	23	77	993,793	1,000,000	–6207
5	2	7	14	77	993,793	1,000,000	–6207
1	1	75	77	77	993,793	1,000,000	–6207
70	5	2	77	775	10,002,463	10,000,000	246
23	16	2	41	775	10,002,463	10,000,000	246
15	10	5	30	775	10,002,463	10,000,000	246
48	20	8	76	7748	99,998,816	100,000,000	-12

*$\delta_T = R_C - R_T$ is the difference between the target resistance value R_T and the nominal value R_C of the graphene QHARS.
*$= m_1 + m_2 + m_3$ is the total number of Hall bars for the graphene Y-Δ array device.

Two types of graphene Y-Δ array device were fabricated, as shown in Fig. 2. Figure 2(a) shows a (25,2,1) Y-network with $R_C = 77 \frac{h}{2e^2}\,\Omega$ (≈ 1 MΩ) and Fig. 2(d) is the optical image of the graphene device corresponding to this design. Figure 2(b) shows a five-arm network combining the Y-networks (3, 3, 8) and (31, 31, 8), where the virtual resistor between terminals A and B is $\widetilde{R}_{AB} = 78 \frac{h}{2e^2}\,\Omega$ (≈ 1 MΩ), the virtual resistor between terminals A' and B' is $\widetilde{R}_{A'B'} = 7750 \frac{h}{2e^2}\,\Omega$ (≈ 100 MΩ), and the virtual resistor between terminals A' and B, or between A and B', is $\widetilde{R}_{AB'} = \widetilde{R}_{A'B} = 778 \frac{h}{2e^2}\,\Omega$ (≈ 10 MΩ). This design leverages a shared parallel array consisting of 8 Hall bars for arm C. Figure 2(e) is the optical image of the graphene device corresponding to it. A 150 nm-thick NbTiN film is deposited on the graphene array devices for the interconnections[21].

The design in Fig. 2(b) can be further developed to produce additional virtual resistors by adding nodes D, E, D' and E'. For example, connecting the nodes D, E, and E' will generate a quantized resistance of $\widetilde{R}_{EE'} = 39 \frac{h}{2e^2}\,\Omega$ (≈ 50 kΩ), as shown by the table in Fig. 2(c). In fact, the multiple-arm network presents a programable QHARS that can be operated with a scanner to select the terminals for desired resistance.

X-ray photoelectron spectroscopy (XPS) element region scans were performed on the test sample to determine the composition (Fig. 3(a)) of the NbTiN film for the superconducting wiring. Elements detected were Nb, Ti, N, and O. Adventitious (surface) C and trace Si (substrate) were also detected but not counted for composition. Region scans for Ti 2p and Nb 3 d



m_1	m_2	m_3	m	m_{WD}	R_C (Ω)	R_T (Ω)	δ_T (μΩ/Ω)
25	2	1	28	77	993 793	1 000 000	-6207
3	3	8	14	78	1 006 699	1 000 000	6699
3	31	8	42	778	10 041 182	10 000 000	4118
31	31	8	70	7 750	100 024 629	100 000 000	246
15	1	1	17	31	400 099	400 000	246
19	1	1	21	39	503 350	500 000	6699

Fig. 2 | Graphene QHARS based on Y-Δ transformation. a Schematic diagram of a (25,2,1) Y-Δ array device. **b** Schematic diagram of a multiple-arm QHARS. The blue dashed network indicates the nodes available for additional resistance values. **c** Examples of the virtual resistances that can be measured from the diagram in (**b**). **d** Optical image of the fabricated graphene Y-Δ array device in (**a**). **e** Optical image of the fabricated graphene Y-Δ array device in (**b**) (with only nodes A, B, C, A' and B'). The orange squares in (**d**) and (**e**) outline the series connection and the parallel connection, respectively.

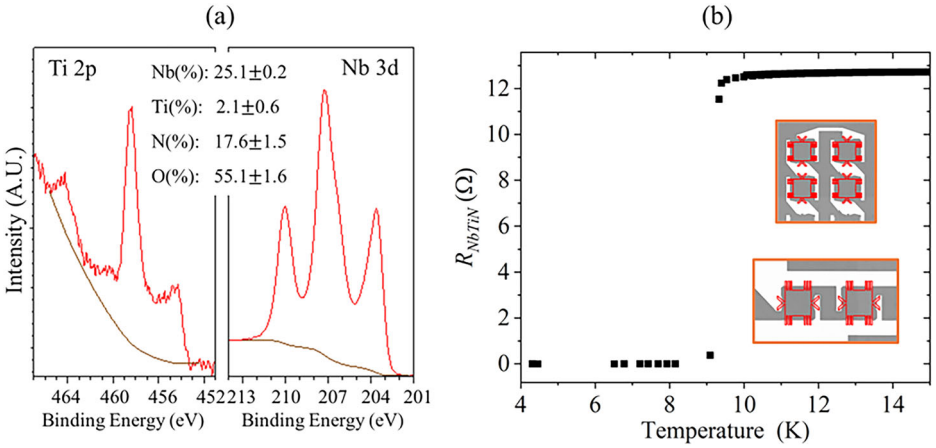


Fig. 3 | Characterization of NbTiN interconnection. a XPS region scans of the NbTiN film for Ti 2p and Nb 3 d. Inset: composition for Nb, Ti, N, and O. **b** Resistance of a NbTiN film deposited on silicon carbide substrate at the same time as the samples are fabricated. Inset: The zoom-in images for series area (top) and the parallel area (bottom) marked by the orange rectangles in Fig. 1(d), 1(e).

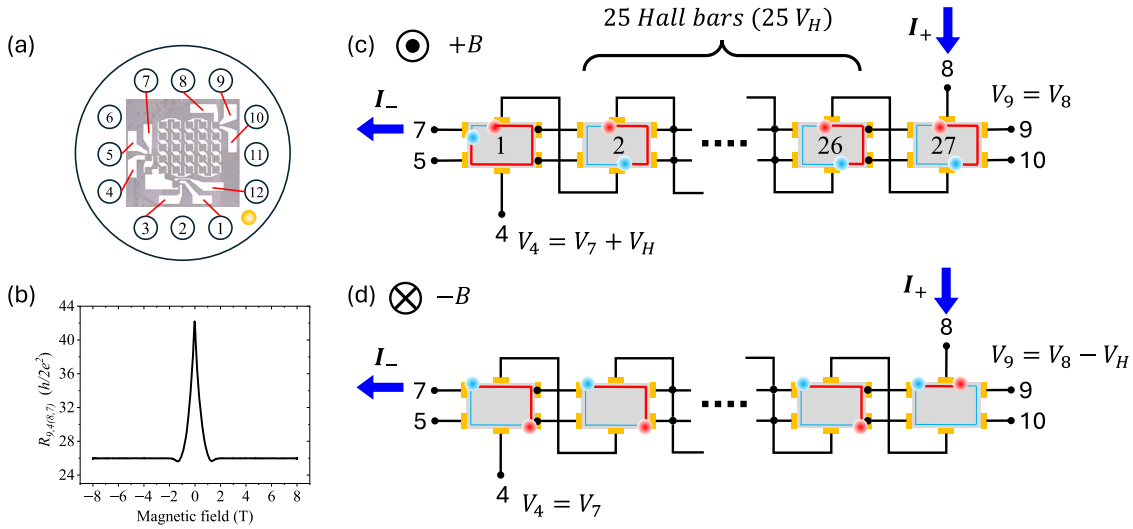


Fig. 4 | Magnetoelectrical transport of graphene Y-Δ array in series mode (scenario-1). a Diagram of the wire bonding for sample (25,2,1). **b** Magnetoresistance of the 27-element array between nodes A and B, obtained with the four-terminal measurement setup in (**c**) and (**d**). **c**, **d** Four-terminal measurement diagrams with schematics of the hotspots and equipotential edges in positive and negative magnetic fields, respectively.

are shown in Fig. 3(a) where peaks arising from several oxidation states are evident. XPS is very surface sensitive, and it is expected that the oxide peaks indicate surface oxidation. The ratio of Nb:Ti was found to be 92:8 (± 2%). The measured critical temperature of the NbTiN film on a control sample is around 9 K, as shown in Fig. 3(b). At 2 K, its critical current is 500 μA at 9 T, which increases to 600 μA at 5 T, and 670 μA when magnetic field is absent.

In the following sections, we first present the magnetoelectrical transport characterization of the (25,2,1) device illustrated in Fig. 2(a) when it is operated under the series mode (node C floating). We then report the precision measurements of three identical (25,2,1) devices when they are operated in the Y-Δ mode (node C grounded). All measurements in this section are done at about 1.6 K in a liquid-helium cryostat, while graphene is *n*-doped.

Magnetoelectrical transport of graphene Y-Δ array devices (series mode)

Characterization of the graphene Y-Δ array device in the series mode requires careful analysis of the high and low equipotential edges of the Hall elements. Figure 4(a) shows a (25,2,1) device that is mounted on a TO-8 (transistor outline) sample holder. The three contact pads of the last Hall bar in arm A (Hall bar no. 1 in Fig. 4(c)) are bonded to pins (4, 5, 7), forming the node A; the three contact pads of the last Hall bar in arm B (Hall bar no.27 in Fig. 4(c)) are bonded to pins (8, 9, 10), forming the node B; the three contact pads of the single Hall bar in arm C are bonded to pins (1, 3, 12), forming the node C. The transport measurements in this session are accomplished by a Keithley 2612B SourceMeter, which is used for both direct current sourcing and voltage measurement.

Figure 4(b) shows the magnetoresistance measurement of the 27-element array between nodes A and B, $R_{9,4(8,7)} = \frac{V_{9,4}}{I_{8,7}}$, measured with the configurations in Fig. 4(c) and 4(d), where the current flows from pin 8 to pin 7 and voltage is probed across pin 9 (V_+) and pin 4 (V_-). In magnetic field above 3 T, $R_{9,4(8,7)}$ is quantized at $26R_H$ instead of $27R_H$. The missing R_H can be explained by the diagram of equipotential edges of the Hall bars, as shown in Fig. 4(c) and 4(d).

When the current flows from pin 8 to pin 7 and the positive magnetic field is pointing out of the plane (Fig. 4(c)), the hotspot of high potential (red dot) in each Hall bar occurs at the right side of the contact where the current flows in, while the hotspot of low potential (blue dot) occurs at the left side of the contact where the current flows out. The side of the contact is determined along the current flowing direction. If three contacts are connected to each other, they can be viewed as a single contact for the convenience to identify the hotspots. The equipotential edges in each Hall bar are therefore outlined by the red and blue lines for high and low equipotential, respectively (referring to Fig. S1 for details). After identifying the equipotential edges in all 27 Hall bars, it is clear that $V_9 = V_8$ and $V_4 = V_7 + V_H$,

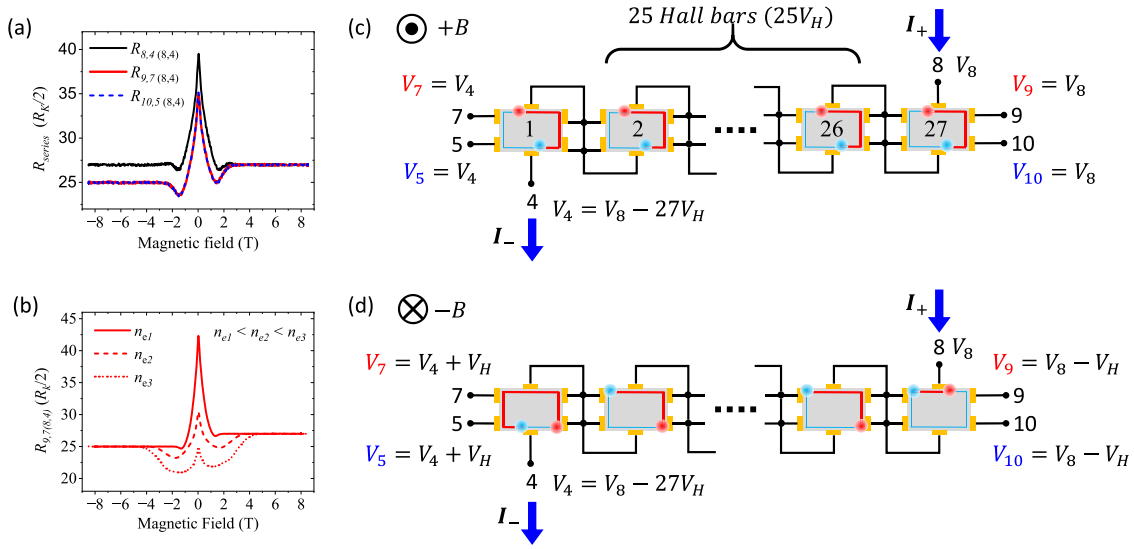


Fig. 5 | Magnetoelectrical transport of graphene Y-Δ array in series mode (scenario-2). a, **b** Magnetoresistance measurement across electrodes (8-4), (9-7), and (10-5) while current flows from 8 to 4, corresponding to the black, red, and blue data sets, respectively. **c**, **d** Analysis of the equipotential edges for the Hall bars when current flows from pin 8 to pin 4.

leading to $V_9 - V_4 = 26V_H$. The contact and wiring resistance can be ignored as they have been effectively mitigated by the superconducting interconnections[21]. Here, $V_H = I_{8,7} \times R_H$ is the voltage drop across the high equipotential and low equipotential edges in individual Hall bar. Figure 4(d) shows hotspots and the equipotential edges of the Hall bars in the reversed magnetic field. In this case, $V_9 = V_8 - V_H$ and $V_4 = V_7$, leading to $V_9 - V_4 = 26V_H$. Despite the magnetic field direction, the voltage across the pin 9 and pin 4 ($V_{9,4}$) does not include the voltage drop across one of the end Hall bars (skipping Hall bar No.1 in positive B and skipping Hall bar No. 27 in negative B), explaining the missing R_H in Fig. 4(b).

Figure 5 shows a different scenario of the magnetoresistance of the 27-element array, where the current flows from pin 8 to pin 4, and the voltage is probed at three different pairs of contacts. The black curve in Fig. 5(a) represents the two-terminal measurement of the magnetoresistance $R_{8,4(8,4)}$, which is quantized at $27R_H$ at magnetic fields above 3 T in both directions. In contrast, the magnetoresistance $R_{9,7(8,4)}$ and $R_{10,5(8,4)}$, obtained through four-terminal measurements (solid red and dashed blue lines in Fig. 5(a)) are quantized at $27R_H$ in a large positive magnetic field but at $25R_H$ in a large negative magnetic field. Applying similar exercise to identify the equipotential edges in the Hall bars, as shown in Fig. 5(c), it is clear that $V_{9,7}$ and $V_{10,5}$ include the voltage drop across all 27 Hall bars in positive large magnetic field. In negative large magnetic field, as shown in Fig. 5(d), neither $V_{9,7}$ nor $V_{10,5}$ includes the voltage drop in Hall bars No.1 and No. 27, explaining the observation of the $25R_H$ plateau. Figure 5 (b) shows the magnetoresistance $R_{9,7(8,4)}$ measured at various electron density values n_{e1}, n_{e2}, and n_{e3}.

Dual source bridge measurement of graphene Y-Δ array devices (Y-Δ mode)

The dual source bridge is analogous to a Wheatstone bridge, where the main ratio arms have been replaced with programmable voltage sources (Fig. S2(a))[38,39]. Like in a Wheatstone bridge, the detector uses either current or voltage detection[40] to determine the bridge balance. Figure 6 (a) shows the diagram of the dual source bridge to test Y-Δ array devices. Two NIST (National Institute of Standards and Technology) standard resistors, R6 and R7, are used as the standard resistor R_S. Both resistors are kept in the same air bath at 23 °C. Two Fluke calibrators, 5730 A and 5720 A, are used to apply voltage on the Y-Δ array device under test and the standard resistor, respectively. A Keysight 34420 A nanovoltmeter is used for voltage detection, which is less noisy than current detection for nominal resistances of 1 GΩ and below. The three nodes of the Y-Δ array device (A, B, C) are connected to the Fluke 5730 A and the Keysight 34420 A. The voltage sources and detector are controlled by an algorithm that measures the detector voltage near an expected null for five settings of the voltage sources[37]. Voltage source V_X applies a constant voltage (V_{X0}) to the Y-Δ array device while voltage source V_S applies a sequence of five voltages to a standard resistor R_S. From the detector voltage V_D measurements and the five voltages applied to the standard resistor, a linear interpolation is used to determine V_{S0} for the balance condition where $V_D = 0$, where the ratio of the applied voltages is equal to the ratio of the resistance values in the other two arms, $V_{X0}/V_{S0} = R_X/R_S$. The process is repeated for the opposite voltage polarity. A measurement of V_D when $V_X = V_S = 0$ is subtracted from all measurements to remove the detector offset[37]. The value of R_X measured by the dual source bridge, $R_X = \frac{V_X}{V_S} R_S = \frac{V_X}{I_S}$, is the virtual resistance R_C in the Δ network. When the bridge is in balance, the current flowing through R_S equals to the current (I_2) flowing throught R_2 (the series array in the arm B). The Y-Δ array device acts like a current divider in this circuit, where the current (I_1) flowing through R_1 (the series array in the arm A) is divided into I_2 and I_3 (current flwoing through R_3).

Since the magnetic field range for the resistance quantization in graphene is strongly related to its carrier density (Fig. 5 (b)), we conduct the dual source bridge measurement of the graphene Y-Δ array devices when the graphene carrier density is adjusted to between $1 \times 10^{11}\,\mathrm{cm}^{-2}$ and $3 \times 10^{11}\,\mathrm{cm}^{-2}$. The reported carrier density is the average of the measured carrier density in Hall bars No. 1, 27, 28 (Fig. S3). The DSB measurements of three identical (25,2,1) devices, B8, B9 and B11, are reported in this paper. The expected value of R_X is $R_C = 77R_H$. Figure 6 (b) shows the details of the triple-connection to the end Hall bar in each arm, i.e., Hall bars No.1, No. 27, and No.28. The three wires in each triple-connection are connected to a common potential point that is placed as close to the voltage source V_X and the detector as possible, respectively.

Figure 6(c) and 6(d) show the R_C deviation from $77R_H$ for B11 measured by the dual source bridge for single-connection and triple-connection to the ground, respectively. The magnetoresistance measurement in Hall bar No. 1 reveals the graphene carrier density to be $\approx 1.3 \times 10^{11}\,\mathrm{cm}^{-2}$ and the $\nu = 2$ plateau starts at $Bc \approx 3.7$ T. With a single connection to the Hall bar in arm C, the R_C deviation of B11 is more than 100 μΩ/Ω at 8.5 T, which is mainly caused by the resistance of the single wire (Fig. S4). The single wire resistance is about 2 Ω when the device (25,2,1) is cooled to 1.6 K. When the triple-connection is implemented at all three nodes A, B, and C, the R_C deviation of B11 is reduced to below 3 μΩ/Ω at 8.5 T (Fig. 6(d)). The error bars of the DSB measurements in Fig. 6 are reduced approximately 10-fold

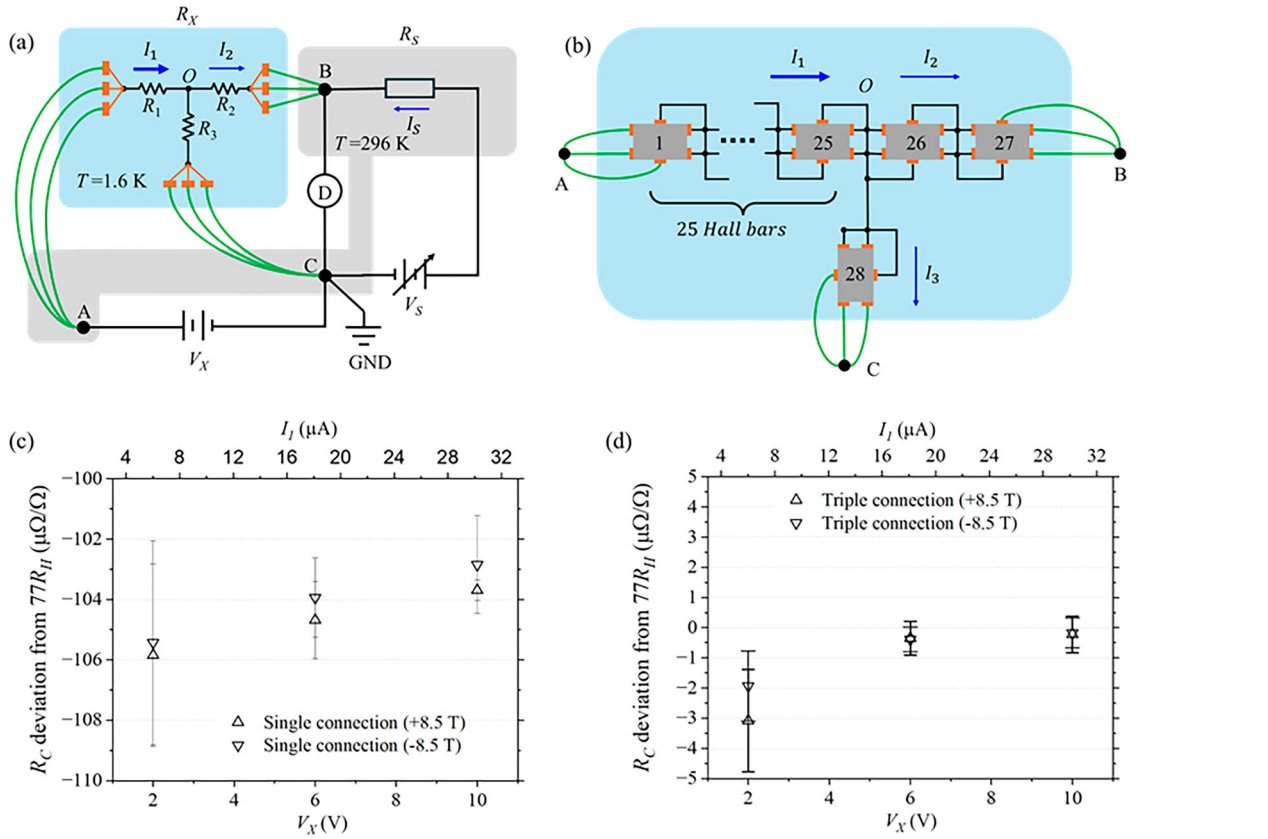


Fig. 6 | Application of triple-connection to graphene Y-Δ array. a Diagram of the DSB measurement to test the Y-Δ array device. The blue shadow marks the low temperature environment in a liquid helium cryostat, while the grey shadow marks the stable temperature environment in an air bath. Unshaded circuits are exposed to ambient environment. **b** Diagram of the triple connections to the graphene Y-Δ array device. **c** Deviation of the R_C of B11 with a single connection to the ground. **d** Deviation of the R_C of B11 with triple connection to the ground. The error bars are type-A uncertainty of the measurements (68.3% confidence interval).

after the temperature controller and the liquid nitrogen monitor for the Janis cryostat are turned off, revealing the uncertainty dominated by the output offset of the voltage sources (Fig. S5).

A substitution method is adopted to eliminate the output offset of the voltage sources, as well as other systematic errors except those caused by short-term instabilities (Table S1). This method involves a baseline, namely R7(R6) in Fig. 7(a), obtained by DSB measurement of the NIST 1 MΩ standard resistor R7 using the other NIST 1 MΩ standard resistor R6 as the standard resistor. The deviation of R7 from its predicted value varies between −0.7 μΩ/Ω and 0.2 μΩ/Ω in the voltage range of 5 V to 25 V, as shown by the black solid circles in Fig. 7(a). The hollow triangles in Fig. 6(a) show the DSB measurements of the B8, namely B8(R6), using also R6 as the standard resistor at magnetic field of +8.5 T (red), +6 T (blue), and +5 T (green), respectively. The deviation of B8 does not exhibit a quantization plateau but tracks the deviation of R7. On the other hand, in Hall bar No.28 of B8, a quantized resistance plateau at R_H has been observed, starting at $B_C \approx 2.5$ T and extending to 8.5 T. Based on the magnetoresistance measurement in Hall bar No. 28, the carrier density is estimated to be about 1.1×10^{11} cm^{-2}. The baseline R7(R6) was obtained three days after the measurements B8(R6).

Subtracting the baseline R7(R6) from B8(R6), we obtain the quantization plateau of B8, as shown in Fig. 7(b). B8 is quantized at $77R_H$ to within 0.1 μΩ/Ω for voltages up to 20 V at the magnetic field of 6 T and 8.5 T. At 25 V, the B8 deviation increases to about −0.27 μΩ/Ω, implying QHE breakdown due to a large current. The current flowing through the 25-element array (I_1) is about 75 μA at 25 V, while the current flowing through the rest of hall bars in B8 is smaller than I_1. When the magnetic field is further reduced to 5 T, the deviation of B8 increases rapidly with increasing voltage above 10 V (Figure S6(a)).

At a similar carrier density level ($\approx 1.2\times10^{11}$ cm^{-2}), B9 is quantized at $77R_H$ to within 50 nΩ/Ω for voltages up to 20 V, but in a wider range of magnetic field, from 5 T to 8.5 T (Fig. 7(c)). At 25 V, the B9 deviation increases to about 0.1 μΩ/Ω, implying QHE breakdown due to a large current. The baseline R7(R6) is obtained just before the measurements of B9(R6). Since the DSB measurements in Fig. 7(b) and (c) agree with each other within the combined uncertainty (see the uncertainty budget table Table S1), we assume that both B8 and B9 are fully quantized at voltages up to 20 V.

Figure 7(d) shows the DSB measurements of B11 that were conducted about 10 months apart. The earlier data (red triangles), with a much larger type A uncertainty sourced from the liquid helium detector and the temperature sensor, show that B11 is well-quantized at 10 V when the carrier density is about 1.3×10^{11} cm^{-2}. At the slightly lower carrier density of about 0.98×10^{11} cm^{-2}, B11 is quantized at +8.5 T while QHE breakdown occurs at −8.5 T (Fig. S6(d)). This observation of QHE breakdown at carrier density lower than 1×10^{11} cm^{-2} is consistent with the experiment results from other groups[8,41].

The uncertainty due to the output offset of the voltage source is effectively canceled out by the substitution method. However, the instability and accuracy of the voltage source in different output ranges still have an impact on the processed data in Fig. 7(b) and 7(c). The voltages applied to the devices and standard resistors are generated in three output ranges of the Fluke calibrators, i.e., 11 V range, 22 V range and 220 V range.

The output range of the voltage source has a strong impact on measurements accomplished within a few hours. In Fig. 8, each data point is an average of measurements in 80 minutes. The time to acquire two adjacent data points measured in the same magnetic field (same magnitude and polarity) is about 3 hours. In the 22 V range, the difference between the two

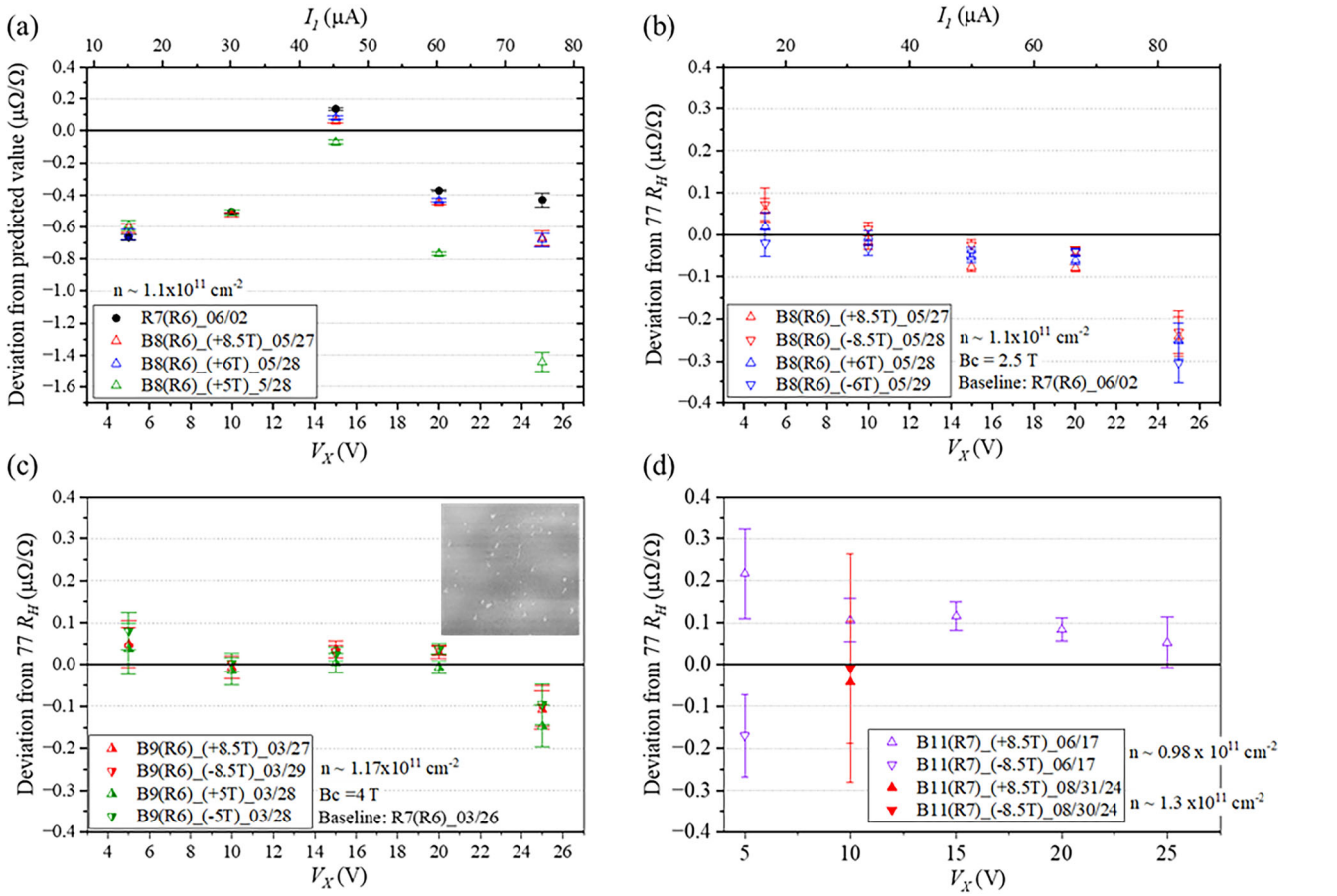


Fig. 7 | DSB measurement results of R_C of three Y-Δ array devices (B8, B9, B11) using NIST 1 MΩ standard resistors R6 and R7. a Deviation of R7 (black solid circles) and the B8 (triangles) from their expected values. The upper axis of all plots is the current flowing through the 25 series array between nodes A and O. **b** Quantization plateau in B8 obtained by subtracting R7(R6) from B8(R6) at +/-8.5 T, +/-6 T and +5 T. **c** Quantization plateau in B9 obtained by subtracting R7(R6) from B9(R6) for +/-8.5 T and +/-5 T. Inset: Optical image (40 μm × 40 um) of the graphene material produced by a confocal laser scanning microscope, showing homogeneous monolayer graphene with a few multilayer graphene patches with brighter contrast[28]. **d** Deviation of B11 from the expected value (77 R_H), averaged for positive and negative field, when their carrier densities are adjusted to a higher level. The error bars are type A uncertainty of the measurements. All data were collected in year 2025, excepted the two solid red triangles in (**d**), which were collected in year 2024. The error bars are type-A uncertainty of the measurements (68.3% confidence interval).

adjacent data points at 15 V and 20 V, measured in the same magnetic field, is within 20 nΩ/Ω. In the 11 V range, the difference between the two data points at 5 V and 10 V, measured in the same magnetic field, is within 80 nΩ/Ω (Fig. 8). Despite the magnitude or the direction of the magnetic field, this observation is highly repeatable in different devices and in measurements that are two months apart, suggesting that the uncertainty due to the instability of the standard resistors and voltage source is within 20 nΩ/Ω for measurements accomplished in a few hours. It also implies that the output errors for the 11 V range and the 22 V range are different. On the other hand, the difference between the two data points measured at the same voltage, but in magnetic field with opposite directions, does not show strong correlation to the voltage range. In Fig. 8(c), this difference is less than 5 nΩ/Ω for both 11 V and 22 V ranges. In Fig. 8(d), this difference is either ≈ 20 nΩ/Ω or ≈ 40 nΩ/Ω (Fig. 8(d)) for both 11 V and 22 V ranges. It could also be smaller in the 11 V range than in the 22 V range (Fig. 8(a)), or vice versa (Fig. 8(b)). Such pairs of data points are measured at least 7 hours apart (Fig. 8(d)) and sometimes about one day or two days apart (Fig. 8(a)-(c)).

When the carrier density of B8 and B9 increases to $2.7 \times 10^{11}\,\mathrm{cm}^{-2}$ and $2.1 \times 10^{11}\,\mathrm{cm}^{-2}$, respectively, both devices are well-quantized at $77R_H$ to within 80 nΩ/Ω in the 22 V range and at 8.5 T (right panel in Fig. 9(a)). Below 7 T, QHE breakdown causes significant deviation in both devices (Fig. S6(b,c)). Three baselines used for the data in Fig. 9(a) are shown in Fig. 9(b). The blue and green solid circles are the baselines for the low carrier density measurements of B8 and B9, respectively, using R6 as the resistor standard. The red solid square is the baseline for the high carrier density measurements of both devices, using R7 as the resistor standard. The DSB measurements of the baselines have a consistent type A uncertainty below 10 nΩ/Ω, as shown by the inset of Fig. 9(b). When replacing one of the standard resistors with the graphene Y-Δ array device, the type A uncertainty increases to 20–50 nΩ/Ω, as shown in Fig. 9(a), due to the higher thermal noise in the phosphorus wires connecting the room temperature cable and the graphene devices at 1.6 K. For example, the resistivity of phosphor bronze wire is about 6.8 times larger than copper wires, leading to about 2.5 times larger thermal noise.

In two sequence days, the baseline measurements may have a discrepancy of 30 nΩ/Ω, as shown by the green solid and hollow circles. The discrepancy of the baseline measurements increases for long-term measurements in weeks or months (comparing the red hollow circle to the blue solid circle), which has been observed to be as large as 150 nΩ/Ω in Fig. 9(b). This is consistent with the maximum discrepancy of the long-term measurements of graphene Y-Δ array devices in Fig. 9(a) and 9(b) (about 160 nΩ/Ω), which is within the uncertainty budget reported in Table S1. In Table S1, we assume that all the Hall bars in the array are fully quantized. Evaluation of the performance of each Hall bar in the array requires more than 100 contact pads, which cannot be done experimentally,

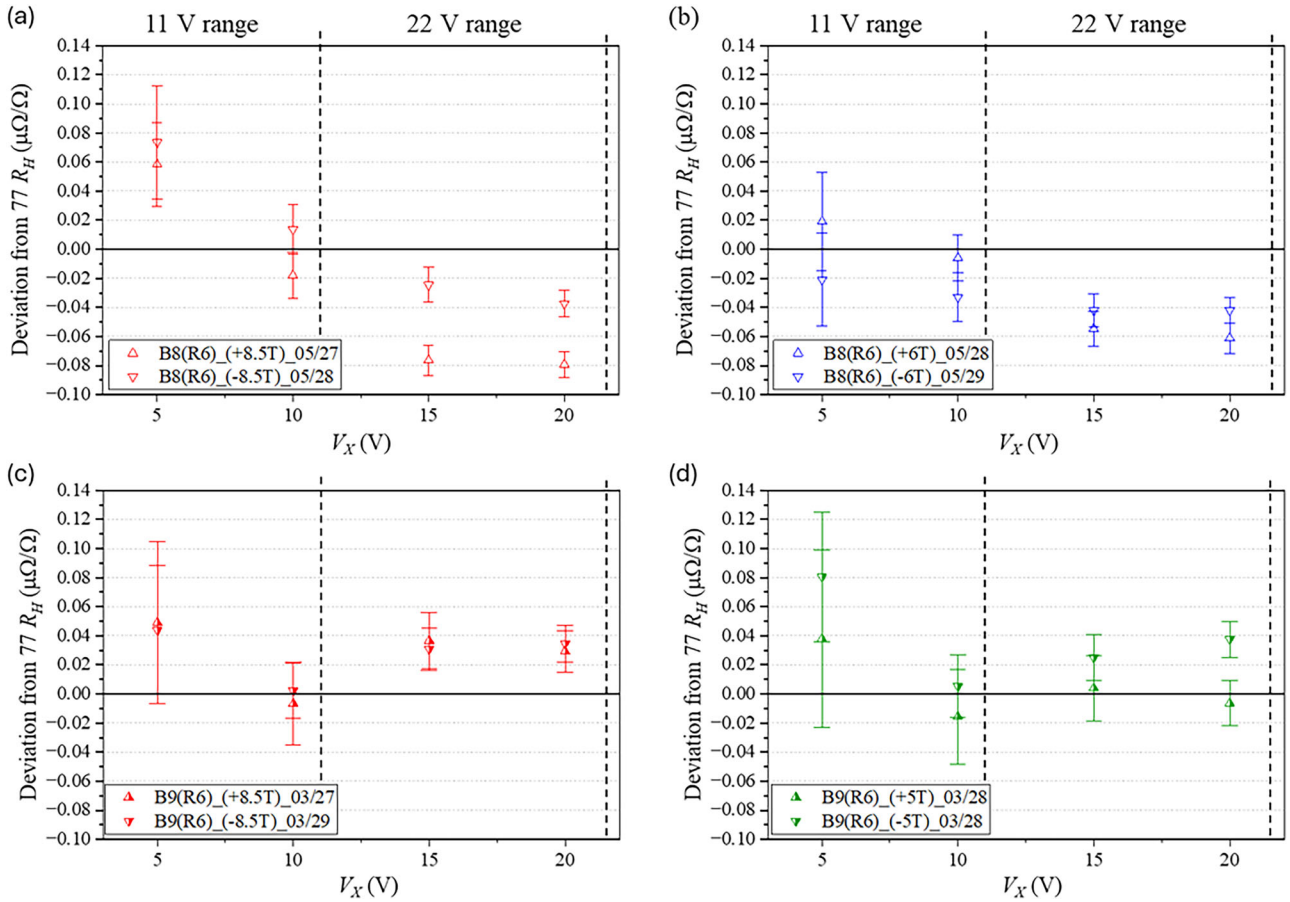


Fig. 8 | The close-up display of the DSB measurements in Figs. 7(b) and 7(c). a DSB measurement of B8 at 8.5 T. **b** DSB measurement of B8 at 6 T. **c** DSB measurement of B9 at 8.5 T. **d** DSB measurement of B8 at 5 T. The error bars are type-A uncertainty of the measurements (68.3% confidence interval).

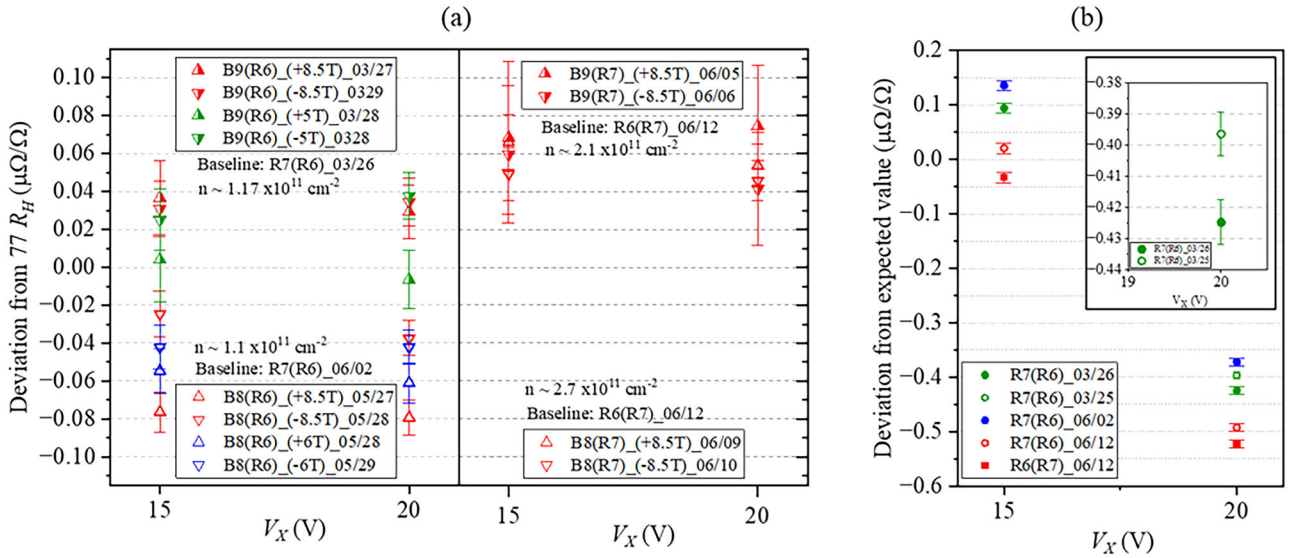


Fig. 9 | DSB measurement of B8 and B9 for different carrier density. a Left panel: DSB measurement of B8 and B9 at lower carrier density around 1×10^{11}cm^{-2}, using R6 as the standard resistor. Right panel: DSB measurement of B8 and B9 at high carrier density of (2 to 3) $\times 10^{11}$cm^{-2}, using R7 as the standard resistor. **b** DSB measurement with 1:1 ratio using R6 and R7. Inset: Two DSB measurements of R7 that are accomplished 24 hours apart. The error bars are type-A uncertainty of the measurements (68.3% confidence interval).

due to the space limitation in the present cryostat and therefore the limited size of the chip. Figure S7 shows the simulated deviation of R_C from $77R_H$ caused by the deviation of R_1, R_2, R_3 and R_{SHB} (quantum Hall resistance of each Hall bar).

Discussion

This work reports a high-accuracy, invariant, high-resistance standard in the MΩ range without using a cryogenic current comparator. Instead, using a dual source bridge, we demonstrated the measurement of $77\frac{h}{2e^2}$ (≈ 1MΩ)

within the uncertainty of 80 nΩ/Ω in graphene quantum Hall array devices at magnetic field as low as 5 T. The minimum operation magnetic field is higher when the carrier density in graphene is larger. The operating temperature of graphene quantum Hall array is mainly decided by the operating temperature of the graphene Hall bar elements in the array and the critical temperature of the superconducting leads connecting the Hall bars. It has been repetitively shown that single Hall bar devices based on epitaxial graphene can be well-quantized above 8 K[6,42]. The critical temperature of the superconducting leads in our samples is around 9 K. In the magnetic field of 9 T, the critical current of our NbTiN film is about 10 mA at 1.75 K and 500 μA at 5 K. Therefore, although the graphene array devices are cooled in a LHe cryostat with base temperature of 1.6 K in this work for demonstration, it is highly promising that the graphene array devices can operate in a cryocoolers without liquid helium. Such an accessible system, consisting of a cryocooler, two voltage sources and a nanovoltmeter, is readily to be adopted in industrial settings to reduce the calibration chain for high resistances in the MΩ range.

We leverage the wye-delta (Y-Δ) transformation to significantly reduce the total number of Hall bars in the graphene array device, bypassing the challenge for homogeneous, high-quality graphene at centimeter scale. Our Y-Δ array device for $77\frac{h}{2e^2}$ (≈ 1MΩ) consists of 28 Hall bar elements, while a device with a series array requires 77 Hall bars to produce the same resistance. By adopting a parallel array for the ground arm in the Y-network, as in the (3,3,8) device, the number of Hall bar elements can be further reduced to realize the quantized resistance near 1 MΩ. Triple connection is the most critical technique to reducing the effect of the contact resistance and lead resistance. The triple connection to the parallel array has been demonstrated by on-chip wire-bonding in our recent work[37]. Our thorough analysis of uncertainty budget identifies the future work to further improve the accuracy of the graphene Y-Δ array devices in the MΩ range.

The Y-network can be modified with multiple arms and additional output nodes, creating a programmable quantum resistance standard that will be a powerful system to minimize the labor and time for high-resistance calibration over a wide resistance range.

Methods

Substrate preparation

The silicon carbide (SiC) wafer was diced into small chips with size of 22.8 mm by 22.8 mm. The SiC chips were cleaned by PG remover, isopropyl alcohol (IPA) and deionized water (DIW) in sequence after dicing. The SiC chips were then immersed in HF solution (100:1) for two minutes, followed by DIW rinsing and blow-dry with nitrogen gas.

Epitaxial graphene synthesis

Graphene reported in this work was grown on the Si-terminated surface of a SiC chip at 1850 °C for 5.5 minutes in an argon background close to atmospheric pressure. The Si-terminated surface was spin-coated with a polymer layer (AZ5214) and placed on a glassy carbon plate with the Si-terminated surface facing down. The polymer AZ5214 was diluted in IPA as AZ5214:IPA ≈ 1 μL:1 mL.

Device Fabrication

All devices were fabricated by maskless lithography, following the process reported in ref.[29]. A thin metal layer of Pd/Au (10 nm/10 nm) was evaporated on the as-grown graphene samples, which prevents graphene from potential contamination during the rest of the fabrication process. A second gold layer (100 nm) was deposited in the designated Hall bar area, followed by an ion milling process applied to the whole substate, carving out graphene Hall bar arrays. Ti/NbTiN (≈ 150 nm) electrodes were deposited through a co-sputter process, where 1.5 A DC current was applied to the Nb target, and 150 W RF power was applied to the Ti target. The Ti adhesion layer was estimated to be about 4 nm. A control sample of NbTiN film was prepared for X-ray photoelectron spectroscopy.

X-ray photoelectron spectroscopy (XPS)

XPS data was collected on the control sample of NbTiN films to determine elemental composition. The x-ray source consisted of 150 W of monochromated 1486.6 eV Al K-α x-rays. Broad scan survey spectra (160 eV pass energy, 0.5 eV step size) as well as higher resolution elemental spectra (20 eV pass energy, 0.1 eV step size) were collected at an angle parallel to surface normal with an analysis area of roughly 700 μm × 300 μm. Analysis was performed using instrument relative sensitivity factors within the CasaXPS Version 2.3.24PR1.0 analysis program. Elements detected were Nb, N, Ti, O as well as adventitious C, and trace Si substrate. All peaks were fit with 70% Gaussian/30% Lorentzian peak shapes. Peak positions were normalized to C 1 s at 284.8 eV. Standard deviations are calculated using two different spots measured as well as potential errors in background subtraction method for Ti.

Data availability

All data supporting the findings of this study are available within the manuscript and the supplementary information files.

Received: 8 September 2025; Accepted: 13 October 2026;
Published online: 09 November 2026

References

1. Klitzing, K. V., Dorda, G. & Pepper, M. New method for high-accuracy determination of the fine-structure constant based on quantized Hall resistance. *Phys. Rev. Lett* **45**, 494–497 (1980).
2. Tsui, D. C., Stormer, H. L. & Gossard, A. C. Two-dimensional magnetotransport in the extreme quantum limit. *Phys. Rev. Lett.* **48**, 1559–1562 (1982).
3. Novoselov, K. S. et al. Two-dimensional gas of massless Dirac fermions in graphene. *Nature* **438**, 197–200 (2005).
4. Chang, C.-Z. et al. Experimental observation of the quantum anomalous Hall effect in a magnetic topological insulator. *Science* **340**, 167–170 (2013).
5. Shi, Q. et al. Odd- and even-denominator fractional quantum Hall states in monolayer WSe2. *Nat. Nanotechnol.* **15**, 569–573 (2020).
6. Ribeiro-Palau, R. et al. Quantum Hall resistance standard in graphene devices under relaxed experimental conditions. *Nat. Nanotechnol.* **10**, 965 (2015).
7. Rigosi, A. F. et al. Graphene devices for tabletop and high-current quantized Hall resistance standards. *IEEE Trans. Instrum. Meas.* **68**(6), 1870 (2019).
8. Yin, Y. et al. Tailoring Permanent Charge Carrier Densities in EpitaxialGraphene on SiC by Functionalization with F4-TCNQ. *Adv. Phys. Res.* **1**, 2200015 (2022).
9. Hu, J. et al. Towards epitaxial graphene p-n junctions as electrically programmable quantum resistance standards. *Sci. Rep.* **8**, 15018 (2018).
10. Delahaye, F. Series and parallel connection of multiterminal quantum Hall effect devices. *J. Appl. Phys.* **73**(11), 7914–7920 (1993).
11. Piquemal, F. P. M., Blanchet, J., Geneves, G. & Andre, J. P. A first attempt to realize (multiple-QHE devices)-series array resistance standards. *IEEE Trans. Instrum. Meas.* **48**(2), 296 (1999).
12. Poirier, W. et al. RK/100 and RK/200 quantum Hall array resistance standards. *J. Appl. Phys.* **92**, 2844–2854 (2002).
13. Hein, G., Schumacher, B. & Ahlers, F. J., *Preparation of Quantum Hall Effect Device Arrays*, presented at Conference on Precision Electromagnetic Measurements, London, UK, 2004 (unpublished).
14. Poirier, W., Bounouh, A., Piquemal, F. & André, J. P. A new generation of QHARS: discussion about the technical criteria for quantization. *Metrologia* **41**, 285–294 (2004).
15. Oe, T. et al. Development of quantum Hall array resistance standards at NMIJ. *IEEE Trans. Instrum. Meas.* **60**(7), 2590 (2011).
16. Oe, T. et al. New design of quantized Hall resistance array device. *IEEE Trans. Instrum. Meas.* **62**(6), 1755 (2013).

17. Lartsev, A. et al. A prototype of RK/200 quantum Hall array resistance standard on epitaxial graphene. *J. Appl. Phys.* **118**, 044506 (2015).
18. Ortolano, M., Abrate, M. & Callegaro, L. On the synthesis of quantum Hall array resistance standards. *Metrologia* **52**(1), 31–39 (2015).
19. Oe, T., Gorwadkar, S., Itatani, T. & Kaneko, N.-H. Development of 1 Mohm quantum Hall array resistance standards. *IEEE Trans. Instrum. Meas.* **66**, 1475–1481 (2017).
20. Oe, T., Gorwadkar, S., Itatani, T. & Kaneko, N.-H., *10 MΩ Quantum Hall Array Device*, presented at Conference on Precision Electromagnetic Measurements, Paris, France, 2018 (unpublished).
21. Kruskopf, M. et al. Next-generation crossover-free quantum Hall arrays with superconducting interconnections. *Metrologia* **56**, 065002 (2019).
22. Oe, T. et al., *Precise evaluation of GaAs/AlGaAs 129 kΩ and 1 MΩ quantum Hall array devices for a quantum Wheatstone bridge*, presented at Conference on Precision Electromagnetic Measurements, Denver, CO, USA, 2020 (unpublished).
23. Panna, A. R. et al. Graphene quantum Hall effect parallel resistance arrays. *Phys. Rev. B: Condens. Matter* **103**, 075408 (2021).
24. He, H. et al. Accurate graphene quantum Hall arrays for the new international system of units. *Nat. Commun.* **13**, 6933 (2022).
25. Jarrett, D. G. et al. Graphene-based star-mesh resistance networks. *IEEE Trans. Instrum. Meas.* **72**, 1502710 (2023).
26. Kruskopf, M. et al. Comeback of epitaxial graphene for electronics: large-area growth of bilayer-free graphene on SiC. *2D Mater* **3**, 041002 (2016).
27. Yang, Y. et al. Epitaxial graphene homogeneity and quantum Hall effect in millimeter-scale devices. *Carbon* **115**, 229–236 (2017).
28. Panchal, V. et al. Confocal laser scanning microscopy for rapid optical characterization of graphene. *Commun. Phys.* **1**(1), 83 (2018).
29. Yang, Y. et al. Low carrier density epitaxial graphene devices on SiC. *Small* **11**(1), 90–95 (2015).
30. He, H. et al. Uniform doping of graphene close to the Dirac point by polymer-assisted assembly of molecular dopants. *Nat. Commun.* **9**(1), 3956 (2018).
31. Kruskopf, M. & Elmquist, R. Epitaxial graphene for quantum resistance metrology. *Metrologia* **55**, R27 (2018).
32. Kennelly, A. E., Equivalence of triangles and stars in conducting networks. *Electrical World and Engineer*, 413-414 (1899).
33. Yu, K. M., Kim, W. S., Lee, S. H., Han, K. S. & Kang, J. H. A method for measuring high resistances with negligible leakage effect using one voltage source and one voltmeter. *Meas. Sci. Technol.* **25**, 075012 (2014).
34. Yu, K. M., Jerrett, D. G., Rigosi, A. F., Payagala, S. U. & Kraft, M. E. Comparison of Multiple Methods for Obtaining PΩ Resistances with Low Uncertainties. *IEEE Trans. Instrum. Meas.* **69**, 3729–3738 (2020).
35. Yu, K. M., Kang, J. H., Lee, S. H., Joo, S. J. & Lee, H. Development of Wye–Delta-Type High-Resistance Standards in the Range of 1 MΩ to 1 GΩ. *J. Electr. Eng. Technol.* **17**, 1987–1992 (2022).
36. Alexander-Webber, J. et al. Giant quantum Hall plateaus generated by charge transfer in epitaxial graphene. *Sci. Rep.* **6**(1), 30296 (2016).
37. Marta, M. et al. Implementation of a 1GΩ star-mesh graphene quantized Hall array resistance standard network for high resistance calibration. *IEEE Trans. Instrum. Meas.* **74**, 1–12 (2025).
38. Henderson, L. C. A. A new technique for the automated measurement of high valued resistors. *J. Phys. E: Sci. Instrum.* **20**, 492–495 (1987).
39. Jarrett, D. G. Automated guarded bridge for calibration of multi-megohm standard resistors from 10 Mohm to 1 Tohm. *IEEE Trans. Instrum. Meas.* **46**(2), 325–328 (1997).
40. van der Beek, J. H. N. & Rietveld, G. Automated high-ohmic resistance bridge with voltage and current null detection. *IEEE Trans. Instrum. Meas.* **62**(6), 1760–1765 (2013).
41. Yin, Y. et al. Graphene quantum Hall resistance standard for realizing the unit of electrical resistance under relaxed experimental conditions. *Phys. Rev. Appl.* **23**, 014025 (2025).
42. Couëdo et al. Robust quantum Hall resistance standard from uniform wafer-scale epitaxial graphene on SiC. *Appl. Phys. Lett.* **128**, 034005 (2026).

Acknowledgements

No funding was received for this research. We greatly appreciate the beneficial discussion with Dr. David B. Newell and Dr. Frank C. Seifert.

Author contributions

W-C. Lin, T. Oe, M. Musso, Dean Jarrett, A. Panna, K. L. Steffens, N.T.M. Tran, O. Massimo, C-H. Yang, C-T. Liang, A.F. Rigosi, R.E. Elmquist, and Y. Yang reviewed the manuscript. D. Jarrett, R.E. Elmquist, and Y. Yang designed the experiment. Y. Yang synthesized graphene material and designed the graphene Y-Δ array devices. W-C. Lin and Y. Yang fabricated the devices. K.L. Steffens conducted the X-ray spectroscopy measurement. W-C. Lin, M. Musso, D. Jarrett, and O. Massimo tested the DSB circuit. M. Musso and D. Jarrett developed the algorithm and code for the DSB measurement program. W-C. Lin, T. Oe, D. Jarrett, C-H. Yang, and Y. Yang tested the graphene devices. W-C. Lin, T. Oe, M. Musso, D. Jarrett, A. Panna, N. T. M. Tran, O. Massimo, Y. Yang contributed to data analysis. T. Oe, A. Panna, D. Jarrett, and Y. Yang contributed to the uncertainty budget.

Funding

The authors received no specific funding for this work.

Competing interests

Y.Y. holds shares in the company Graphene Waves. C-.T.L. is a Guest Editor of Semiconductor Science and Technology/Focus Collection on Quantum Semiconductor Research and Technology in Taiwan. C-.T.L. was not involved in the journal's review of, or decisions related to, this manuscript. The other authors do not have a competing interest.

Additional information

Supplementary information The online version contains supplementary material available at https://doi.org/10.1038/s41699-026-00749-3.

Correspondence and requests for materials should be addressed to Yanfei Yang.

Reprints and permissions information is available at http://www.nature.com/reprints

Publisher's note Springer Nature remains neutral with regard to jurisdictional claims in published maps and institutional affiliations.

Open Access This article is licensed under a Creative Commons Attribution 4.0 International License, which permits use, sharing, adaptation, distribution and reproduction in any medium or format, as long as you give appropriate credit to the original author(s) and the source, provide a link to the Creative Commons licence, and indicate if changes were made. The images or other third party material in this article are included in the article's Creative Commons licence, unless indicated otherwise in a credit line to the material. If material is not included in the article's Creative Commons licence and your intended use is not permitted by statutory regulation or exceeds the permitted use, you will need to obtain permission directly from the copyright holder. To view a copy of this licence, visit http://creativecommons.org/licenses/by/4.0/.

This is a U.S. Government work and not under copyright protection in the US; foreign copyright protection may apply 2026

This Article in Press is shared early to give you faster access to new research. It is citable and carries a permanent DOI. The final edited version will replace it automatically.